
PART II: REFERENCE

Part II of the *CASPR User's Guide* describes data preprocessing and the methods used in the retrieval of surface temperature, surface albedo, atmospheric water vapor, cloud amount, optical depth, particle effective radius, phase, temperature, and pressure, and the surface radiative fluxes. For those algorithms that are published, only minimal algorithm descriptions are given here.

1. PROCESSING OVERVIEW

The overall processing scheme involves six groups of calculations: the cloud mask, clear sky surface parameters, clear sky surface images, cloud parameters, cloudy-sky surface parameters, and radiative fluxes. This order is dictated by the fact that cloud and surface properties are input to the radiative fluxes, and some surface and clear sky properties are required for the cloud retrievals.

If the input land mask only contains LAND and NOTLAND categories, the surface types are refined by using clear sky reflectances and brightness temperatures. LAND and NOTLAND are subdivided into snow-covered and snow-free land, open water, and ice. The clear sky surface temperature and albedo are then computed. Precipitable water is computed from the satellite data if atmospheric temperature and humidity profiles are not present.

Clear sky images for the surface temperature, precipitable water, and channels 2 and 4 values are created by interpolating the clear values to cloudy pixels. These are needed in subsequent calculations of cloud properties, cloudy sky surface temperature and albedo, and radiative fluxes. This is a very important, and usually error prone, step. In situations where cloud cover is extensive, values that are used to fill cloudy pixels may have come from a great distance, and therefore may be significantly different from the true value. Additionally, false identifications of clear pixels (i.e., cloud contamination) can create significant errors.

The cloud particle phase, effective radius, optical depth, temperature, and pressure are computed next. Cloudy sky surface temperature and albedo, then radiative fluxes complete the calculations.

The following sections describe these steps in detail.

2. CONVERSION OF AVHRR CHANNEL INFORMATION

CASPR assumes that all AVHRR channels are calibrated. Standard calibration can be done according to the procedures and data given in the NOAA Polar Orbiter Data User's Guide (NOAA, 1991) and the NOAA KLM User's Guide (<http://www2.ncdc.noaa.gov/docs/klm>). The thermal channel calibration should include the non-linear correction (NOAA, 1991). Channels 1 and 2 should have time-dependent calibrations for NOAAs 7, 9, 11, and 14, and the standard calibration for other satellites. As part of the NOAA/NASA AVHRR Pathfinder Calibration Working Group activities, the in-orbit degradation of channels 1 (0.6 μm) and 2 (0.9 μm), which are not calibrated on-board, has been determined using the southeastern Libyan desert as a time-invariant calibration target. A statistical analysis of the data over the calibration target show that channels 1 and 2 of NOAA 9 had degraded at the rate of 5.9% and 3.5% per year respectively. The relative variations of the gain were anchored to "absolute" calibrations based on concurrent aircraft and satellite measurements made over the White Sands area of New Mexico. Rao (1993) presents simple formulae and a look-up table for the time-dependent calibration of these two channels for NOAA 9; calibration coefficients for other NOAAs 7 and 11 can be obtained from NOAA/NESDIS (M. Jones, pers. comm., 1994), and the method and data for NOAA 14 can be found at <http://orbitnet.nesdis.noaa.gov/ora/text/nrao02.txt>.

The usual calibration methods for channels 1 and 2 do not include a correction for variations in the Earth-Sun distance over the course of the year. Such a correction is optional here, and is done as follows:

$$\alpha' = \alpha \left(\frac{R_{jday}}{R_{mean}} \right)^2 \quad (1)$$

where α' is the corrected albedo, α is the albedo computed using the mean Earth-Sun distance, R_{jday} is the actual Earth-Sun distance for the day of the year $jday$, and R_{mean} is the mean distance.

Three other spectral "images" are required for the retrieval of surface and cloud properties: the reflected portion of channel 3, the differences between channels 3 (3.7 μm) and 4 (11 μm) at night, and the difference between channels 4 and 5 (12 μm). At 3.7 μm , AVHRR channel 3 contains both reflected solar and emitted thermal components. The reflected portion is **approximated** by removing from the total radiance an estimate of the emitted portion, based on the temperature of channel 4 (e.g., Allen et al., 1990):

$$\rho_3 = \frac{L_3 - B_3(T_4)}{L_0\mu - B_3(T_4)} \quad (2)$$

where ρ_3 is the channel 3 reflectance, L_3 is the channel 3 radiance, $B_3(T_4)$ is the Planck function for channel 3 based on the channel 4 temperature T_4 , L_0 is the solar constant for the band (adjusted for Earth-Sun distance), and μ is the cosine of the solar zenith angle. Equation 2 is derived from the basic relationship

$$L_3 = \epsilon_3 B_3(T_4) + \rho_3 L_0 \mu$$

where $\epsilon_3 = 1 - \rho_3$ is the emissivity. This relationship assumes that the surface or cloud in the field-of-view do not transmit any radiation, and that emission and reflection are isotropic. Without any a priori knowledge of the scene, these assumptions are necessary. The difference between channels 4 and 5 and between channels 3 and 4 at night are a simple arithmetic subtraction of brightness temperatures.

3. SURFACE PROPERTIES

SURFACE TEMPERATURE

For the retrieval of clear sky surface temperature a simple regression model is used to correct for atmospheric attenuation. For high-latitude ocean and snow-covered land we use the equation

$$T_s = a + bT_4 + c(T_4 - T_5) + d[(T_4 - T_5)(\sec\theta - 1)] \quad (3)$$

where T_s is the surface temperature, T_4 and T_5 are the satellite measured brightness temperatures in channels 4 and 5, θ is the sensor scan angle, and a , b , c , and d are regression coefficients. To determine the empirical relationship in (3), radiosonde data from drifting ice and land stations in the Arctic and Antarctic were used with a radiative transfer model to simulate the sensor brightness temperatures.

The regression method of relating modeled brightness temperatures to surface temperature was also used for a snow-free land algorithm. But because spectral emissivities for vegetation in channels 4 and 5 are variable and generally unknown, they are variables in the regression. Additionally, scan angle is not a variable in the regression since its dependence on angular emissivity is unknown. The regression equation for snow-free land has the form:

$$T_s = a + bT_4 + cT_5 + d\varepsilon_4 + e\varepsilon_5 \quad (4)$$

where ε_i is the emissivity in channel i . The surface temperature retrieval methods for both sea ice/snow and snow-free land are described in detail in Key, et al. (1997).

The cloudy sky surface temperature calculation is based on empirical (linear regression) relationships between the clear sky temperature, wind speed, and solar zenith angle (daytime), determined using surface observations from the SHEBA (Surface HEat Budget of the Arctic) experiment. **It applies only to sea ice.** The clear sky surface temperatures are interpolated to cloudy pixels with a kriging function, then the cloudy sky temperatures are estimated from these clear temperatures and one or two other variables, depending on the time of year. For the polar night and before the melt season (November through April) there are two equations:

- solar zenith angle 80 degrees or more: $T_{cld} = a_1 + b_1 * T_{clr} + c_1 * u_{cld}$
solar zenith angle less than 80 degrees: $T_{cld} = a_2 + b_2 * T_{clr} + c_2 * \cos(Z) + d_2 * u_{cld}$

During the warm season, defined as May-September with the surface temperature greater than 255K, the following apply:

- solar zenith angle less than 90 degrees: $T_{cld} = a_3 + b_3 * T_{clr} + c_3 * \cos(Z) + d_3 * t_{cld}$
or: $T_{cld} = a_3 + b_3 * T_{clr} + c_3 * \cos(Z)$
- nighttime only: $T_{cld} = a_4 + b_4 * T_{clr} + c_4 * u_{cld}$

where T_{cld} is the cloudy sky surface temperature (K), T_{clr} is the clear sky surface temperature (K), u_{cld} is

the cloudy sky wind speed (m s^{-1}), Z is the solar zenith angle, t_{cld} is the number of hours that it has been cloudy. Because t_{cld} will not generally be known to better than six hours with satellite data, the alternate equation is used in CASPR. This procedure is unpublished.



CAUTION

If you don't have wind speed data, comment out the call to `surftemp_cloudy` in `retrieve.pro`. Using a wind speed of 0 is not a valid workaround! At present this procedure should be considered experimental.



CAUTION

The largest potential source of error in the cloudy sky surface temperature is the interpolation of clear sky values to cloudy areas. This is particularly true for single image processing (as opposed to the time series approach). Cloudy sky results in coastal areas and areas of extensive cloud cover have large uncertainties!

SURFACE ALBEDO

The retrieval of surface albedo involves four steps:

1. Convert channels 1 and 2 narrowband reflectances to a broadband reflectance.
2. Correct the top-of-atmosphere (TOA) broadband reflectance for anisotropy.
3. Convert the TOA broadband albedo to a surface broadband albedo.
4. Adjust the surface clear sky broadband albedo for the effects of cloud cover in cloudy pixels (snow/ice only).

The general methodology described by steps 1-3 was used by Csiszar and Gutman (1999) for global land studies. In CASPR, relationships for land and ocean were developed independent of that study, and methods for snow/ice and ocean were added. DeAbreu et al. (1994), Lindsay and Rothrock (1994), and earlier versions of CASPR used a procedure where the anisotropic reflectance correction was applied to channels 1 and 2, an atmospheric correction was done on those channels, then narrowband albedos were converted to broadband. In CASPR that procedure tended to overestimate the albedo of snow/ice.

It is important to distinguish between "inherent" and "apparent" surface albedos. The inherent albedo is the "true", no-atmosphere, or "black-sky" albedo of the surface and is independent of changes in atmospheric conditions. The apparent albedo is what would be measured by up- and down-looking radiometers in the field. It varies with atmospheric conditions. Both vary with solar zenith angle and are directional in that regard. The difference between them is very small for the ocean but can be large for vegetation and snow. Figure 1 gives an example of the difference between these two albedo types for ocean, vegetation, and snow. As the figure illustrates, differences can be up to 10%. **CASPR calculates the directional-hemispherical apparent albedo**, although it also contains code to calculate the inherent albedo. After the apparent albedo is calculated it is adjusted for cloud cover. The complete procedure is detailed in Key et al. (2001).

The first step is to convert the narrowband reflectances in AVHRR channels 1 and 2 to a TOA

broadband reflectance. This is necessary because the anisotropic reflectance correction in step 2 requires a broadband reflectance. The narrow-to-broadband conversion takes the form

$$\rho_{toa} = a + b\rho_{1,toa} + c\rho_{2,toa} \quad (5)$$

where $\rho_{1,toa}$ is the channel 1 reflectance, $\rho_{2,toa}$ is the channel 2 reflectance, ρ_{toa} is the broadband TOA reflectance, and a , b , and c are regression coefficients. To develop the regression relationship *Streamer* was used to simulate the TOA reflectances over a broad range of viewing and illumination angles, atmospheric conditions (aerosol optical depth and water vapor amount), and surface types and albedos. Separate sets of coefficients were determined for snow/ice and snow-free land (generic vegetation in *Streamer*). For open ocean the broadband reflectance is set to the channel 1 reflectance.

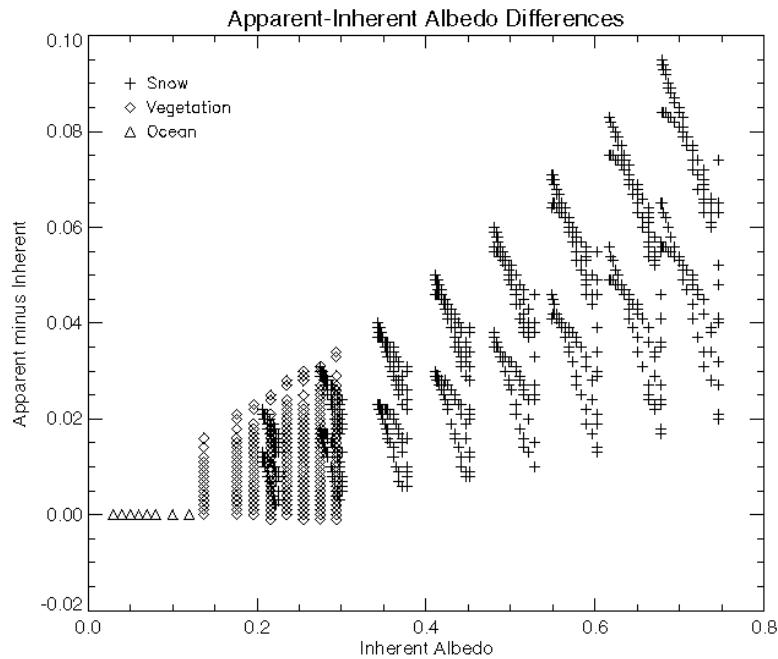


Figure 1. The difference between the apparent (atmosphere dependent) and inherent surface albedos of unfrozen ocean, snow-free land (vegetation), and snow. Data are from radiative transfer model calculations (*Streamer*) for two precipitable water amounts (0.5 and 5 g cm⁻²), two aerosol optical depths (0.05 and 0.5), and solar zenith angles from 0 to 87 degrees.

The next step is to correct for the dependence of the sun-satellite-surface geometry on reflectance. This is done with data presented in Suttles et al. (1988). That study used ERBE and GOES data to determine TOA anisotropic reflectance factors (ARF) for the broad shortwave band over various surfaces. It updates the earlier work of Taylor and Stowe (1984). Both the ERBE and GOES instruments measure radiances and are therefore a function of viewing and illumination geometry. To convert the directional reflectance to albedo, the ERBE/GOES ARFs are used:

$$\alpha_{toa} = \frac{\rho_{toa}}{f} \quad (6)$$

where ρ_{toa} is the reflectance observed at the sensor (simulated by *Streamer* in step 1), f is the anisotropic reflectance factor, and α_{toa} is the TOA albedo, which is only a function of solar zenith angle. A trilinear interpolation routine was used to retrieve f as a function of satellite zenith angle, solar zenith angle, and the relative azimuth angle.

Next, the broadband, clear sky, apparent surface albedo is estimated with a regression relationship of the form

$$\alpha_{toa} = a + b\alpha_s \quad (7)$$

where α_s is the surface reflectance, and a and b are a function of water vapor, aerosol amount, and solar zenith angle. There is a different set of coefficients for each solar zenith angle, aerosol optical depth, and precipitable water bin. This method was used by Koepke (1989) for AVHRR channels 1 and 2 separately. Here the coefficients were determined with *Streamer* for a variety of surface and atmospheric conditions and illumination angles. Viewing geometry is not important in this step. Snow/ice and vegetation surface types were used in the radiative transfer calculations, and the regression coefficients are based on the combined surface type data. For ocean surface albedo a simpler approach is used:

$$\alpha_s = a + b\alpha_{toa} + c\cos Z + dPW + e\tau_{aer} \quad (8)$$

where PW is precipitable water (cm), τ_{aer} is aerosol visible optical depth (unitless), Z is the solar zenith angle, and a , b , c , d , and e are regression coefficient based on modeled albedos.

The surface albedo under clear and cloudy conditions can be very different. This is illustrated in Figure 2 which shows the change in surface albedo with increasing optical depth. The values are fractional change, where 1 means no difference between clear and cloudy values. While the cloudy sky albedo can be 15% more or less than the clear sky value for both surface types, it is consistently higher for snow, with a mean difference near 10%. For vegetation, the cloudy albedo may be higher or lower, so that the mean difference is very small. For this reason, only the snow albedo is adjusted for cloud cover.

The albedo of cloudy pixels is determined using the clear sky albedo, interpolated to fill in the entire image, adjusted by the cloud optical depth and the solar zenith angle. This conversion is also based on model calculations, where *Streamer* was used to compute upwelling and downwelling fluxes for a snow/ice surface over a range of cloud and atmospheric conditions. The empirical relationship between the clear sky broadband albedo, cloud optical depth, and the cloudy sky broadband surface albedo is

$$\alpha_{s, cld} = a + b\alpha_{s, clr} + c\ln(\tau + 1) + d\cos Z \quad (9)$$

where τ is the cloud visible optical depth (unitless), $\alpha_{s, clr}$ is the clear sky **apparent** albedo (see above), Z is the solar zenith angle, and a , b , and c are regression coefficients. As aerosol and water vapor amounts are not explicit in this relationship, this adjustment assumes that their effect on the surface albedo is small relative to that of clouds. Note, however, that this adjustment is to the apparent albedo, which is a function of aerosol and water vapor amounts. No distinction is made between water and ice clouds, although both were included in the model data for the regression analysis. This relationship works best when the snow surface is bright ($\alpha > 0.5$) and clouds have small to moderately large optical depths ($1 < \tau < 50$). For snow-free land and open water the cloudy sky broadband albedo is set to the clear sky broadband value.

In the model calculations of steps 1, 3, and 4, the variable ranges were as follows: solar zenith angle: 0 - 87 degrees, aerosol visible optical depth: 0.05 - 0.5, precipitable water: 0.5 - 5 g m⁻³, snow visible albedo: 0.5 - 0.99, and vegetation visible albedo: 0.07 - 0.15. In all cases ozone amount was prescribed at

325 Dobson units.

Note: No albedo retrievals are done for solar zenith angles greater than the variable DARKZEN, which is currently set to 85 degrees. Figure 3 shows the latitudes and times of the year where solar zenith angles greater than 85 degrees are experienced. Surface albedo retrievals will not be done for latitudes above the dashed line on a particular day.



CAUTION

The largest potential source of error in the cloudy sky surface albedo is the interpolation of clear sky values to cloudy areas. This is particularly true for single image processing (as opposed to the time series approach). Cloudy sky results in coastal areas and areas of extensive cloud cover have large uncertainties!

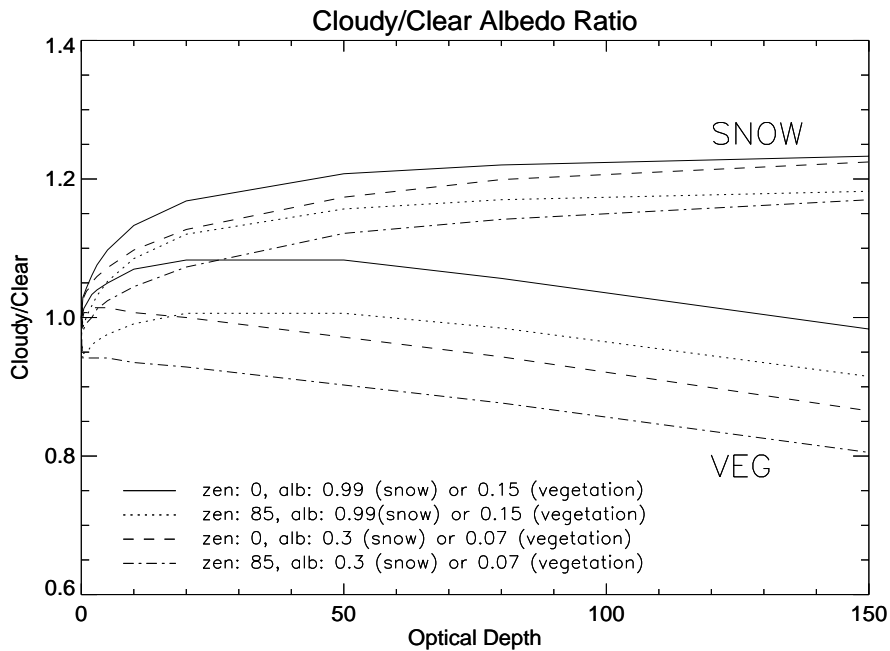


Figure 2. Differences between clear and cloudy surface albedos expressed as a fraction (cloudy divided by clear; 1 means no difference) for snow (top set of lines) and generic vegetation (bottom set), given as a function of cloud optical depth. Results were generated with a radiative transfer model for water and ice cloud under varying atmospheric conditions. The lines are for different solar zenith angles (0 and 85 degrees) and visible surface albedos (0.3 and 0.99 for snow; 0.07 and 0.15 for vegetation).

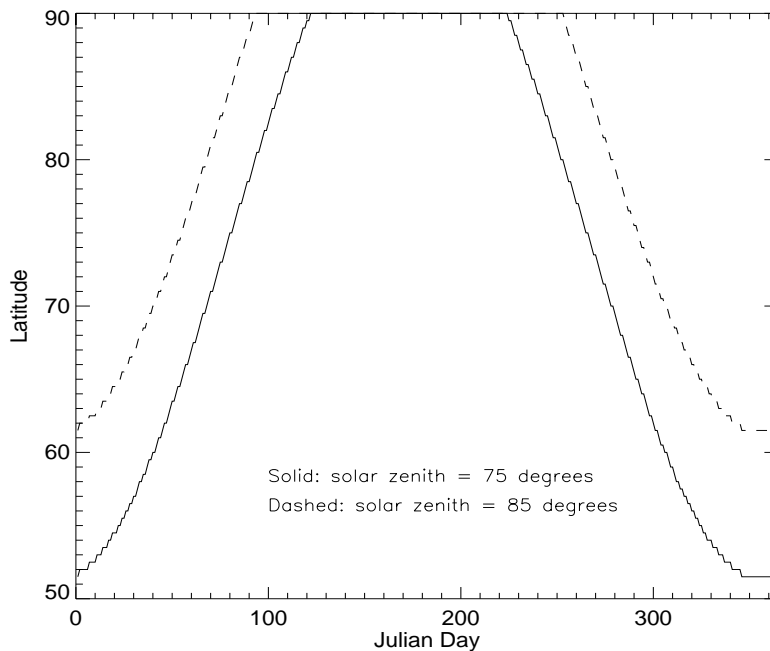


Figure 3. Latitudes and times of the year where zenith angles greater than 85 degrees and greater than 75 degrees are experienced at solar noon. All latitudes poleward of those shown will have solar zenith angles larger than 85 or 75 degrees. The 85 degree line is relevant to albedo retrievals; the 75 degree line is relevant to cloud optical depth retrievals.

4. WATER VAPOR

The total precipitable water in the atmospheric vertical column is needed for the surface albedo, cloud optical depth, and radiative flux calculations. It may be computed from the humidity profile, if available, or estimated from the satellite data using the split-window thermal channels. The preferred method is to compute it from the humidity profile, and that will be done if it is available. **This split-window technique has a large uncertainty**, as neither of the channels are very sensitive to water vapor (which is why they are window channels!).

The procedure is to convert relative humidity to mixing ratio, then integrate mixing ratio over all layers, using the mean of two adjacent levels as the representative value of the layer:

$$PW = 100 \sum_{i=1}^{n-1} \frac{w}{g\rho} (p_i - p_{i+1}) \quad (10)$$

where PW is precipitable water (cm), w is the mixing ratio (g/g), g is gravitational acceleration (9.8 m s^{-2}), ρ is the density of water (1000 kg m^{-3}), p is pressure (Pa), and n is the number of vertical levels with $i=1$ being the surface.

If the humidity profile is not available, the precipitable water will be estimated for clear sky areas using the AVHRR thermal channels. At high latitudes the relationship is:

$$PW = \exp[-10.4974 + 0.751008(T_4 - T_5) + 0.0453005T_5] \cos \theta \quad (11)$$

where PW is precipitable water (cm), T_4 and T_5 are the satellite measured brightness temperatures in channels 4 and 5, and θ is the sensor scan angle. The coefficients were determined over a range of surface temperatures and water vapor amounts typical of the Arctic using modeled AVHRR radiances as in the surface temperature algorithm. This procedure is for clear-sky pixels only. It is far less reliable (and more variable) than using a humidity profile.

5. CLEAR SKY COMPOSITES

A critical step in time series cloud detection, and an optional step in single image processing, is clear sky compositing. This involves creating a clear sky image for various channels or parameters, which means filling in cloudy areas with clear values. This is a very important, and usually error prone, step. In situations where cloud cover is extensive, values that are used to fill cloudy pixels may have come from a great distance in space or time, and therefore may be significantly different from the true value.



CAUTION

The largest potential source of error in the cloudy sky surface temperature and albedo is the interpolation of clear sky values to cloudy areas. This is particularly true for single image processing (as opposed to the time series approach). Cloudy sky results in coastal areas and areas of extensive cloud cover have large uncertainties!

This step is necessary for two reasons: (1) In time series cloud detection the clear sky images are used in a final thresholding operation, where the actual radiance data are compared to the estimated clear sky values and a new cloud/not-cloud determination is made. (2) The retrieval of some cloud properties, and the calculation of surface radiative fluxes, require values for the surface under the cloud.

In time series cloud detection, and optionally with single-image processing (see the keyword *clear_composite*), clear sky statistics are compiled for each pixel using all clear values within some distance of the pixel and over some number of days (typically 150x150 km cells and 5 days). Medians of the required channels and parameter data are computed. If a cell occurs along a coastline, only pixels with the same surface type (LAND or NOTLAND) as the center pixel are used. Pixels in the clear sky composite that did not have medians assigned due to the lack of clear values are filled by a kriging interpolation procedure. The probability of finding clear pixels can be increased by enlarging the cell size or using more days, but doing so also increases the variability and may adversely affect the next step.

The compositing procedure therefore involves two steps: computing median values for each pixel over a small region in space and time, and filling in those pixels that did not receive a clear sky estimate with an interpolation procedure. In time series cloud masking both are an integral part of the procedure; they are not optional. But after the cloud detection step, whether in time series mode or not, clear sky compositing can be done (again, see the *clear_composite* keyword). The filling/interpolation will be done whether or not clear compositing is done, the only difference being that in one case the clear images are based on clear values from the current image only; in the other case it is based on clear values from the current and previous images.

If clear sky compositing is done, the maximum clear sky channel 4 temperature is written to a separate file. This can be used to improve single image cloud detection via the *tsurfest* keyword to *caspr*. See the section on *File Input and Output* in the *User's Guide* for more information.

6. CLOUD PROPERTIES

RADIATIVE TRANSFER MODEL

Cloud detection and the retrieval of cloud optical depth and particle effective radius rely heavily on modeled TOA albedo and brightness temperature. Before detailing those procedures, the radiative transfer model *Streamer* (Key and Schweiger, 1998) is briefly described. TOA radiances (intensities) are computed for use in the cloud property retrievals while irradiances (fluxes) are computed in order to examine the surface radiation budget. For radiances *Streamer* uses the discrete ordinate solver DISORT described in Stamnes et al. (1988). For irradiances the two-stream method following Toon et al. (1989) is employed. In both cases there are 24 shortwave and 105 longwave spectral bands. Gas absorption for water vapor, ozone, CO₂ and oxygen is parameterized using an exponential sum fitting technique (Tsay et al., 1989).

Cloud optical properties are based on parameterization schemes from three different sources. For water clouds, the data are taken from Hu and Stamnes (1993). Effective radii range from 2.5 to 60 μm for shortwave and longwave portions of the spectrum. For ice clouds in the shortwave the parameterization of Fu and Liou (1993) is used. Longwave ice cloud optical properties are based on Mie calculations using spherical particles. This parameterization is unpublished but follows the methodology of Hu and Stamnes. Both the water and ice cloud parameterizations are based on the empirical relationship between the particle effective radius and extinction, single scatter albedo, and the asymmetry parameter.

CLOUD DETECTION

Methods of detecting clouds in satellite data range from simple thresholding procedures to complex neural networks. No attempt is made here to survey the tremendous breadth of this field; instead, a few examples from the literature are given. Ebert (1987) described one of the first polar-specific cloud retrieval algorithms, one that utilized a variety of spectral and textural measures. Key and Barry (1989) implemented a high-latitude method similar to that used in the global algorithm of the ISCCP (Rossow and Garder, 1993) based on spectral, spatial, and temporal variations of clouds. A number of studies have exploited the high reflectivity of liquid water clouds at 3.7 μm during the day (e.g., Allen et al, 1990; Welch et al., 1992; Sakellariou et al., 1993), while only a few have been developed specifically for nighttime retrievals (e.g., Yamanouchi et al., 1987). Most of the cloud detection algorithms are based on empirical relationships derived from a small sample of satellite data.

The cloud masking procedure presented here consists of thresholding operations that are based on modeled sensor radiances. The AVHRR radiances are simulated for a wide variety of surface and atmospheric conditions, and values that approximately divide clear from cloudy scenes are determined. Examples are given in Figures 4 and 5 where the channel 3 reflectance and the thermal channel differences, respectively, are shown as a function of cloud optical depth. Clear sky is represented as having a cloud optical depth of zero.

Single-Image Masking

The underlying philosophy of the single-image cloud detection procedure is that it should work as well as possible without requiring ancillary information. The target user is one who has a few individual images that are not necessarily part of a time series, and no additional information such as model fields of surface temperature or an elevation database. The single-image cloud mask procedure could be certainly be improved with such information, but it would be unreasonable to require it.

The single image cloud mask uses four primary spectral tests and an optional secondary test. Many of

the cloud test concepts can be found in the Air Force SERCAA procedures (Gustafson et al., 1994); some appear in the NOAA CLAVR algorithm (Stowe et al., 1991); most were developed and/or used elsewhere but refined and extended for use in the polar regions. The application of the spectral tests is conceptually simple: initialize the cloud mask to clear, then apply the spectral cloud tests to label cloudy pixels. The primary spectral cloud tests are described in the following paragraphs. Only two of the four tests are applied under all solar zenith angle (SZA) conditions. One is used only when it is dark; the other is used only when it relatively bright. See Table 1 for SZA cutoffs.

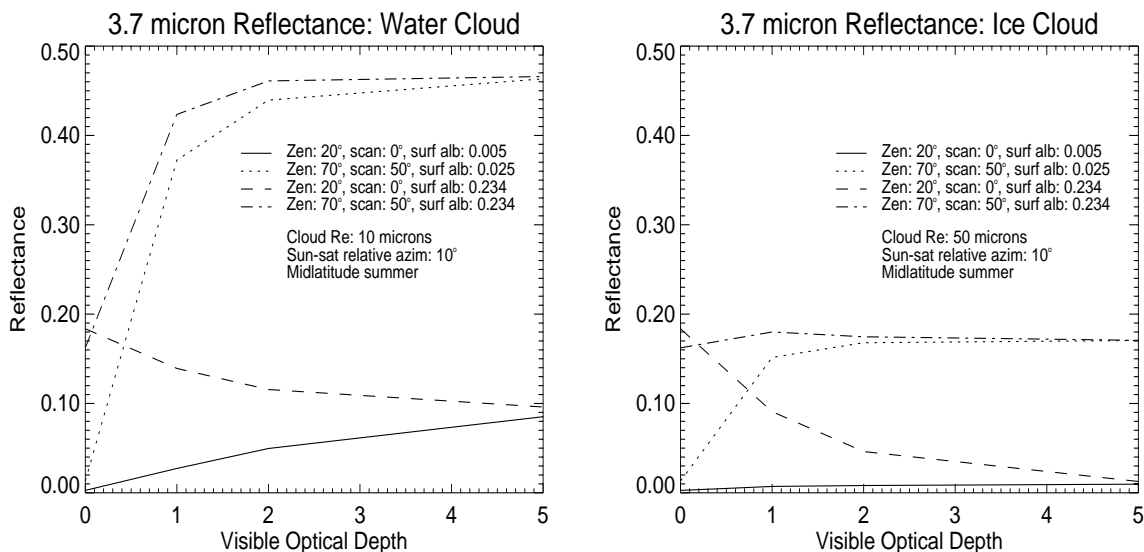


Figure 4. Channel 3 reflectance as a function of liquid (often simply "water") cloud optical depth for a variety of surface and viewing conditions.

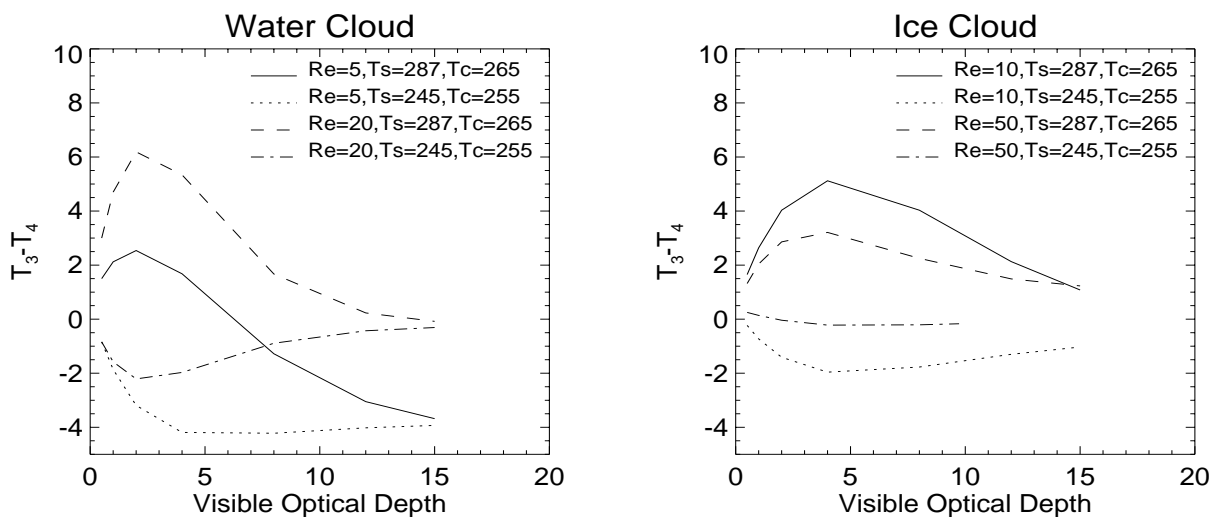


Figure 5. The brightness temperature difference (BTD) of AVHRR channels 3-4 as a function of cloud optical depth for water cloud (left) and ice cloud (right). T_c is the cloud top temperature, Re is the cloud particle effective radius.

Cloud Tests

Split-Window Cirrus test, 11-12 μm (all SZA) - Ice clouds absorb and scatter less at 11 μm than at 12 μm , so their transmittances are higher at 11 μm . Water clouds also absorb less at 11 μm but they scatter more. Nevertheless, both ice and liquid clouds have higher transmittances at 11 μm . For cold cirrus clouds and thin water clouds the result is higher brightness temperatures at 11 μm . However, water vapor affects this difference and must be considered. This is accomplished indirectly through the use of the scan angle and brightness temperature. The BT45 differences are corrected for viewing angle effects before being used in any of the cloud tests. Individual pixels are labeled as cloudy if the corrected btd45 is greater than the CT_THRESH thresholds (Table 2).

CT_THRESH values are from Saunders and Kriebel (1988) for temperatures of 260 K and greater, with minor adjustments at the low end of the temperature range. For lower temperatures the table was extended by simulating clear sky values with *Streamer* and adding a small offset to account for unmodelled effects. The nadir thresholds are shown in Figure 6. A function that adjusts for the scan angle dependence of BT45 was then determined empirically, with the same functional form as that given by Yamanouchi et al. (1987):

$$BTD45' = BTD45 - \frac{(23.6 - ZC)(1 - \cos\theta)}{1 - 0.1589(1 - \cos\theta)} \quad (12)$$

where ZC is given in Table 2, BTD45 is the unadjusted brightness temperature difference, and θ is the scan angle. This effectively adjusts the raw brightness temperature difference to a nadir view. The angle adjustment functions are shown in Figure 7. Note that the sign of the correction changes at approximately 260 K. If BTD45' is greater than CT_THRESH then the pixel is cloudy. The model simulations assumed that the surface emissivities were the same at 11 and 12 μm . This is probably not the case for snow, so the thresholds are increased by 0.3 K if the surface is known to be snow. This correction should actually be done to radiances, as the emissivity effect is nonlinear in brightness temperature.

Warm clouds, 11-12 μm (all SZA) - The transmittance relationships described in the previous test hold true regardless of the relationship between the cloud and surface temperatures. For warm clouds BTD45 may be negative, so an additional test is required (cf., Yamanouchi et al., 1987). A pixel is considered to be cloudy if $BTD45' < WT_THRESH$ (Table 2; Figures 6 and 7). Temperature inversions and warm clouds are ubiquitous during the polar night, but also occur at other times of the year and in other locations outside of the polar regions; e.g., over cold ocean currents.

Water cloud test, 1.6 and 3.7 μm (SZA < NOREFZEN) - The single-scattering albedo of small droplets at 1.6 and 3.7 μm (AVHRR channels 3A and 3B) is considerably larger than that of ice crystals, including snow on the surface. Therefore, the 1.6 and 3.7 μm reflectances are very high relative to snow, open water, and vegetation. For sunlit scenes the application of reflectance tests depends on the solar zenith angle. For solar zenith angles less than DAYZEN (Table 1) constant thresholds in channels 1 and 3 are applied. A pixel is considered cloudy if $REF3 > REF3_OCEAN$ and $REF1 > REF1_OCEAN$ or $REF3 > REF3_LAND$ and $REF1 > REF1_LAND$, where REF1 and REF3 are the channels 1 and 3 reflectances. There are actually REF3_OCEAN and REF3_LAND variables for the 3.7 and 1.6 μm channels, channels 3B and 3A, respectively: REF3A_OCEAN, REF3B_OCEAN, REF3A_LAND, and REF3B_LAND. The channel referenced by "3B" is channel 3 through NOAA-15 and channel 3B on NOAA-16 and beyond. The visible reflectance test reduces the mislabelling of clear snow-free land and silty water (near mouths of rivers) pixels which have relatively high reflectances at 3.7 microns.

If the zenith angle is between DAYZEN and NOREFZEN then these thresholds are scaled, increasing as a function of the zenith angle. A function was derived empirically:

$$REF3' = REF3 + \left(a \frac{REF3ADD}{b} \right) \quad (13)$$

where REF3' is the adjusted threshold, REF3 and REF3ADD correspond to ocean or land types (Table 1; REF3*_ADD), $a=(\text{SZA}-\text{DAYZEN})^3$, and $b=(90-\text{DAYZEN})^3$. The same adjustment is done for the channel 1 reflectance. A pixel is cloudy if it's reflectance is greater than REF3' or REF1'. No reflectance tests are applied to for zenith angles between NOREFZEN and NIGHTZEN. *Note: This effect is still under investigation.*

Low stratus-thin cirrus tests, 3.7-11 μm (SZA \geq NIGHTZEN) - Both ice and water clouds have lower emissivities at 3.7 μm than at 11 or 12 μm . Additionally, small droplets scatter much more efficiently at 3.7 μm than at 11 or 12 μm . For optically thick water clouds, where transmittance is small, this translates into a lower brightness temperature in channel 3. Stratus clouds often exhibit this effect, as do thin, warm clouds (less frequent). For thin, cold clouds the brightness temperature at 3.7 μm can be greater than that at 11 μm because of transmitted radiation from the warm surface in the shorter wavelength band. This is typical of cirrus clouds. A pixel is cloudy if $\text{BTD34} \leq \text{LSTTCI_34LO}$ or $\text{BTD34} \geq \text{LSTTCI_34HI}$, where BTD34 is the brightness temperature difference between channels 3 and 4. Due to the large amount of noise in channel 3 at low temperatures, this test is only performed for temperatures greater than MINTEMP.

Cloud Cloud - Surface Temperature Tests, 11 μm or T_s (all SZA regions) - These tests are intended to detect very cold clouds by comparing the 11 μm brightness temperature to either a climatological surface temperature or a surface temperature estimate. The cold cloud over oceans test is most useful during the summer months at night. It has little effect in the winter or during the daytime, when reflective tests work well. In some sense it performs in a manner similar to the MODIS CO2 high cloud test. It tends to find the cold, optically thick clouds that the thin cirrus, warm cloud, and low stratus tests miss. It is a simple threshold test that utilizes a monthly climatological estimate of the lowest expected surface temperature over the ocean (frozen or unfrozen). If the 11 μm temperature is less than the climatological minimum surface temperature, the pixel is cloudy.

The other cloud cloud - surface temperature test relies on an estimate of the surface temperature input by the user, and is only performed if an estimate of the surface temperature (or 11 μm brightness temperature, both are treated equally) is provided. It is a simple threshold test such that any pixel with an 11 μm brightness temperature less than 20 K below the surface temperature estimate is considered to be cloudy. This is most useful at night during the winter when some optically thick, cold clouds are misidentified as clear sky.

Clear Tests

To account for potential problems with the cloud tests, particularly the 11-12 μm BTD, tests that confidently identify clear pixels are used. The clear tests are only applied to those pixels labelled CLOUDY by the cloud tests.

Low NIR reflectance test (DAY and HISZA regions): This test is the complement of the reflectance cloud test, where pixels with 1.6 or 3.7 μm reflectances less than $REF3*0.4$ are considered clear.

NDSI test (DAY and HISZA regions): The Normalized Difference Snow Index (NDSI; Hall et al.) is used in conjunction with the NIR reflectance for the AVHRR/3 with the 1.6 μm channel (NOAA-16 and higher). If NDSI is large and the NIR reflectance is small, then the pixel is clear. NDSI is calculated as

$$NDSI = \frac{\rho_1 - \rho_3}{\rho_1 + \rho_3} \quad (14)$$

Rethresholding

The secondary threshold test is a rethresholding operation using only the channel 4 brightness temperatures. It is not employed by default in CASPR, but is available as an option. Using pixels labeled as clear by the primary tests, an average channel 4 temperature image is constructed with a kriging procedure for small regions (200 km over land; 300 km over ocean). During the day ($SZA \leq NOREFZEN$) the 95th percentile clear sky temperature is used; during dim and dark conditions ($SZA > NOREFZEN$) the median is used. During the day, if the channel 4 temperature is more than DEL4DAY degrees less than the clear temperature then it is cloudy. While this test works well in identifying thin cirrus, it results in some false detections near coastlines, and in areas with large variability in elevation it may actually create more problems than it solves. During dim and dark conditions when temperature inversions and warm clouds are common, the test is two-sided. If the channel 4 temperature is more than DEL4LO degrees less than the clear temperature or if it is DEL4HI degrees greater than the clear temperature then it is cloudy.

At night this rethresholding can be important for two reasons: (1) there is less spectral information available and (2) AVHRR channel 3 tends to be noisy at low temperatures, common during the polar night. Concerning the available spectral information, under most conditions optically thick clouds simply cannot be distinguished from clear sky with the three thermal channels alone. This is illustrated for a few cases in Figure 5. The result is false clear detections, i.e., cloudy pixels labeled as clear. Concerning noise in channel 3, it generally results in predictable errors - false cloud detections - so that those pixels not labeled as cloudy by the primary cloud tests are usually clear. So the primary spectral cloud tests at night are expected to result in some false detections for noisy pixels and for optically thick clouds.



CAUTION

At night, the cloudier the image, the longer the computation time (unless only spectral tests are being done), and the more uncertain the results.

The thresholds can be adjusted collectively through the *threshadj* keyword to the procedures **caspr** and **cloudmask_1**. This keyword allows the user to adjust the algorithm to be "cloud-conservative" or "clear-conservative". The cloud/clear-conservative decision is necessary because there will always be partly cloudy pixels, mixed phase clouds, mixed clear pixels, etc. that do not fall neatly into one class or the other. However, this is somewhat crude in that not all thresholds scale linearly. For best results, change the individual thresholds until the desired results are achieved. The *threshadj* keyword is used in the single-image cloud masking mode when clear parameters are computed. A second, clear-conservative mask is generated to increase the likelihood that those pixels labeled as clear actually are clear.

It is assumed here that we have no a priori knowledge of surface characteristics (e.g., surface temperature from the previous day) and no a priori knowledge of the the location of snow/ice. In fact, the only distinction between surface types is land and ocean. Land may be snow-free or snow-covered. Ocean can be open water or sea ice. Additionally, the nighttime procedure does not incorporate any surface type distinction. This severely limits single-image cloud masking accuracy. Having such information would allow the use of additional spectral cloud tests (e.g., the channel 2/1 ratio over snow-free land), and would allow "tighter" thresholds.

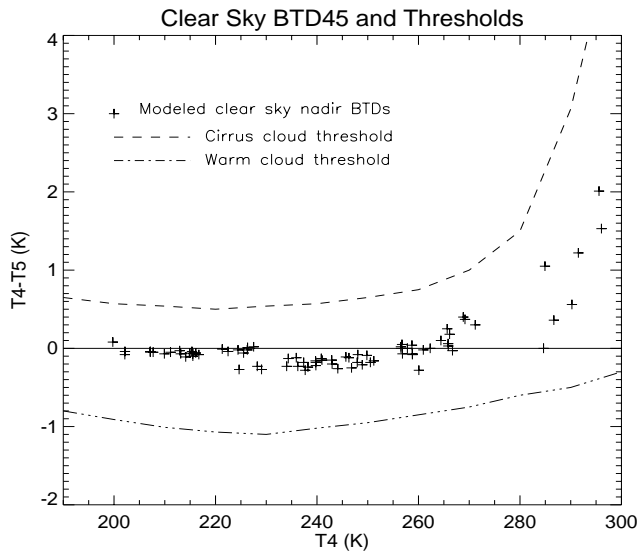


Figure 6. Modeled (*Streamer*) clear sky brightness temperature differences (plus signs) the the cirrus and warm cloud test thresholds (dashed and solid lines, respectively).

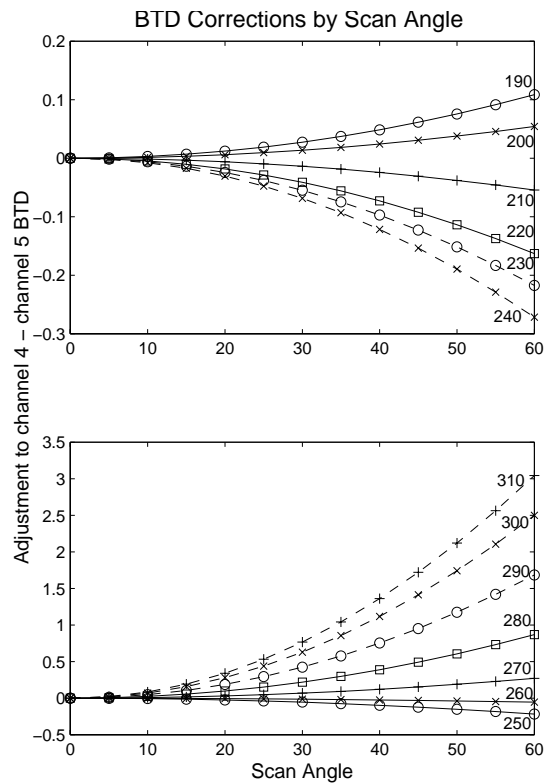


Figure 7. Brightness temperature difference dependence on scan angle. These functions are used to adjust brightness temperature differences before application of the cirrus and warm cloud tests.

Table 1. Thresholds used in cloud detection.

Threshold Variable	Value
DAYZEN	60
NOREFZEN	85
NIGHTZEN	88
DEL4DAY	8.0
DEL4LO	4.0
DEL4HI	4.0
REF3A_OCEAN	0.04
REF3B_OCEAN	0.1
REF1_OCEAN	0.35
REF3A_LAND	0.40
REF3B_LAND	0.09
REF1_LAND	0.35
REF3A_OCEAN_ADD	0.0
REF3B_OCEAN_ADD	0.0
REF3A_LAND_ADD	0.15
REF3B_LAND_ADD	0.15
REF3A_SNOW_ADD	0.5
REF3B_SNOW_ADD	0.5
REF1_OCEAN_ADD	0.10
REF1_LAND_ADD	0.15
LSTTCI_34LO	-1.0
LSTTCI_34HI	3.5

Table 2. Brightness temperature difference thresholds for the cirrus cloud test as a function of temperature (K).

	190	200	210	220	230	240	250	260	270	280	290	300	310
CT_THRESH	0.45	0.37	0.34	0.34	0.34	0.40	0.50	0.75	1.00	1.50	3.06	5.77	9.41
WT_THRESH	-0.8	-0.91	-1.01	-1.07	-1.1	-1.02	-0.95	-0.85	-0.75	-0.6	-0.5	-0.3	-0.15
ZC	23.4	23.5	23.7	23.9	24.0	24.1	24.0	23.7	23.2	20.5	19.7	19.0	18.0

Time Series Masking

The time series cloud masking procedure operates on a sequence of images acquired on consecutive days at approximately the same solar time. It first applies spectral tests for an initial labeling of cloudy and clear pixels, then further refines the identification of clear pixels by examining changes in spectral characteristics from one day to the next. The clear pixels that result from these spectral and temporal tests are used to construct a clear sky radiance statistics over some number of days for various spectral channels. The statistics are then used in a final thresholding operation to label/relabel pixels as either clear or cloudy. More specifically the steps are:

1. Apply the single-image cloud mask procedure to identify pixels that are likely to be cloudy. This alleviates the problem of persistent cloud being labelled as clear in the time tests.
2. Examine the time change in spectral characteristics between pairs of days. A pixel is clear if the spectral tests (step #1) say it not cloudy and if it varies little from one day to the next. The channel 4 brightness temperature and the adjusted brightness temperature difference (4-5) are used in the dark parts of the image; these plus the channel 1 reflectance, and the channel 3 reflectance are used in the sunlit portions. Table 3 give the thresholds used in this step (TIME*).
3. Clear sky statistics are compiled for each pixel using all clear values within some distance of the pixel and over some number of days (typically 150x150 km cells and 5 days). Medians of the channels 1 and 3 reflectances (day only) and the channel 4 temperature (day and night) are computed. If a cell occurs along a coastline, only pixels with the same surface type (LAND or NOT-LAND) as the center pixel are used. Pixels in the clear sky composite that did not have medians assigned due to the lack of clear values are filled with a kriging interpolation scheme. The probability of finding clear pixels can be increased by enlarging the cell size or using more days, but doing so also increases the variability and may adversely affect the next step.
4. The clear sky composite statistics are used in a final threshold operation to label or relabel all pixels as clear or cloudy. A pixel can be labeled as cloudy if its brightness temperature is higher or lower than its mean clear value plus or minus, respectively, some value that reflects the natural variability for clear sky, or if its reflectance in either channel 1 or 3 (daytime) is higher than its mean clear reflectance plus (not minus) some value (DEL* in Table 3). However, the single-image spectral tests are run again in cloud-conservative mode and those pixels labelled as cloudy will also be cloudy in the final mask. This implies higher confidence in the spectral tests (with cloud-conservative thresholds) than in the final thresholding operation.

This scheme can be tuned by modifying the following: (1) single-image cloud mask spectral cloud test thresholds (file **cldmask1.pro**, (2) *ndays* (number of days in the clear sky compositing), *cellrad* (radius of cells for clear statistics), *MINCLEAR* (minimum number of clear values needed for statistics in a

cell), and *threshadj* in the calls to **cloudmask_1** (procedures **cloudmask_n** and **final_threshold**); *ndays* and *cellrad* most directly control the number of values that go into the clear sky statistics, (3) time thresholds (procedure **clear_pairs**), and (4) standard deviations multipliers (procedure **final_threshold**).

Cloud masks for images at the beginning and end of the time series have a much larger uncertainty than those at least *ndays/2* places away from the ends. This results from the first and last few images being at the beginning or end of the *ndays* images on which the clear sky statistics were based. For example, given *ndays* = 5, the cloud mask for the first image is determined from the final thresholding based on clear sky statistics over days 1-5. The cloud mask for the third image is based on statistics from the same period. Obviously, the statistics are more representative of the third image of the first.

Table 3. Time and final thresholds used in cloud detection.

Threshold Variable	Value
TIMETHRESH3A	0.06
TIMETHRESH3B	0.04
TIMETHRESH1	0.07
TIMETHRESH4_LAND	3.0
TIMETHRESH4_OCEAN	2.0
TIMETHRESH45_LAND	0.40
TIMETHRESH45_OCEAN	0.35
DEL4LO_OCEAN	3.0
DEL4HI_OCEAN	3.0
DEL4LO_LAND	4.0
DEL4HI_LAND	4.0
DEL4LO_SNOW	6.0
DEL4HI_SNOW	6.0
DEL1	0.07
DEL3A_OCEAN	0.06
DEL3A_LAND	0.08
DEL3B_OCEAN	0.045
DEL3B_LAND	0.055

CLOUD PARTICLE PHASE

This section describes the algorithms used in the determination of cloud particle phase. In CASPR, all clouds are composed of either liquid droplets ("water cloud") or solid ice crystals ("ice cloud"). No attempt is made to identify mixed-phase or multilayer clouds. The theoretical background for these procedures is detailed in Key and Intrieri (2000). Only a partial description is given here.

The determination of cloud particle phase, liquid or solid (generally referred to as "water" and "ice"), is based on both physical and spectral properties. Physically, liquid cloud droplets can exist at temperatures as low as -40 C, perhaps even lower, although clouds are likely to be composed of both liquid droplets and ice crystals at temperatures below -10 C. The spectral difference between water and ice clouds occurs because of differences in absorption and scattering. Based only on the imaginary index of refraction, which is an indicator of absorption, more absorption will take place in ice clouds at 11 and 12 μm than in water clouds, so brightness temperature differences between 3.7 and 11 or 12 μm will be larger for ice clouds. However, absorption alone does not provide enough information to explain observed spectral differences. The single scattering albedo indicates how effective a volume of particles are at scattering incident radiation. Unlike the imaginary index of refraction, it applies to size distribution of particles. Scattering is greater at 3.7 μm than at 11 or 12 μm and the smaller the particle, the greater the scattering. But for typical ice crystals sizes there is very little difference in scattering across this portion of the spectrum. Furthermore, the single scattering albedo indicates that during the day, ice clouds will exhibit a lower reflectance at 3.7 μm than water droplets. At visible wavelengths, the single scattering albedo of both water and ice clouds is near unity and absorption is near zero.

For optically thick clouds, where the transmittance is near zero and the surface contribution to upwelling radiance is small, absorption and scattering define the spectral characteristics of a cloud. We expect the brightness temperature difference between channels 3 and 4 (BTD34) to be negative for water clouds with small effective radii. For thick ice clouds with particle effective radii of 30 μm or larger, the single scattering albedo indicates that BTD34 would be near zero. This is, in fact, the case, as demonstrated by the model calculations (*Streamer*) presented in Figure 7. Both plots show that for visible optical depths τ greater than 5, water cloud BTD34 is negative while ice cloud differences tend to be positive, at least for smaller water droplets and larger ice crystals. For larger optical depths BTD34 for ice clouds decreases. For optically thin clouds the transmissivity is not negligible and the surface temperature influences the brightness temperature measured at the satellite. BTD34 for cold water clouds (surface is warmer than the cloud) is positive when the optical depth is small. BTD34 for ice clouds takes on larger positive values in these cases. The opposite occurs for warm ice clouds, where BTD34 is negative.

The brightness temperature difference between 11 and 12 μm , BTD45, is much smaller than BTD34 for both water and ice clouds, and there is considerable overlap in BTD45 for the two phases (Figure 8). The absolute value of BTD45 increases as cloud optical depth decreases (not shown). Therefore, large BTD45 differences (positive or negative) indicate thin clouds.

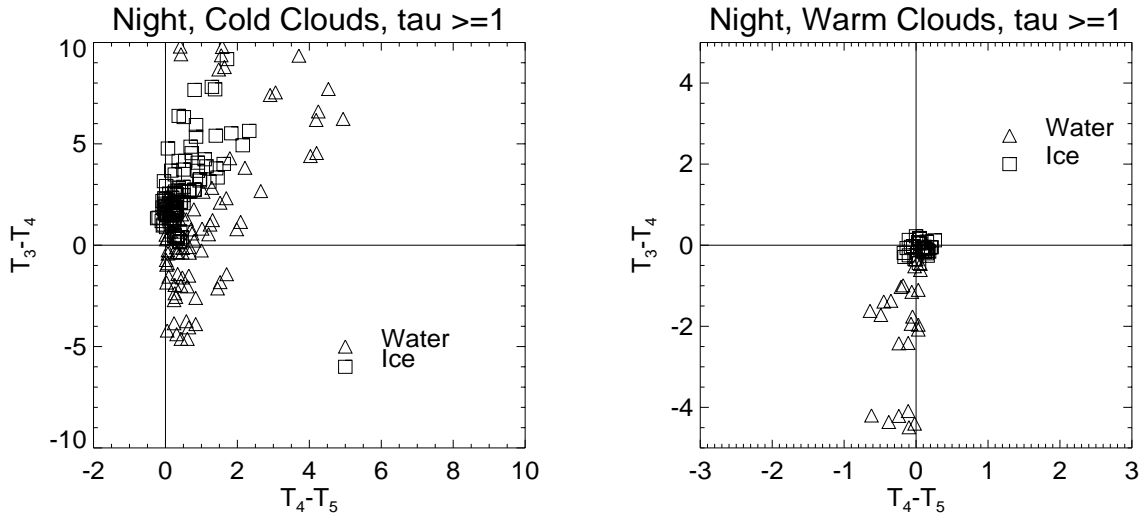


Figure 8. Modeled brightness temperature differences for AVHRR channels 3 minus 4 (3.7 minus 11 μm) and channels 4 minus 5 (11 minus 12 μm) for water and ice clouds. The visible optical depth for the data shown is one or greater. Water clouds have top temperatures greater than 250 K; ice clouds are less than 270 K. Calculations were done for tropical, midlatitude, and arctic conditions.

In the presence of solar radiation, the single scattering albedo at 3.7 or 1.6 μm is the primary spectral feature used in distinguishing ice and water cloud. Ice particles do not scatter as efficiently as water droplets at this wavelength, due to both their indices of refraction (the real part) and the fact that ice clouds are typically composed of larger particles, which scatter less efficiently, than water clouds. However, the actual reflectance depends not only on particle phase, but also on viewing and illumination geometry and surface reflectance. This is illustrated in Figure 9, which shows the 3.7 μm (NOAA-15 and earlier) and 1.6 μm (NOAA-16 and later) modeled reflectances as a function of the scattering angle. The scattering angle ψ is the angle between the incident and reflected beams:

$$\psi = 180 - \text{acos}(\cos\theta_{sun} \cos\theta_{sat} + \sin\theta_{sun} \sin\theta_{sat} \cos\phi) \quad (15)$$

where θ_{sun} is the solar zenith angle, θ_{sat} is the satellite zenith angle, and ϕ is the relative azimuth angle (where 0 is looking away from the sun and 180 is looking into the sun); all angles are in degrees. A scattering angle of 0° implies forward scattering; 180° means backscattering. The figure gives reflectances for cloud visible optical depths between 2 and 5, and for snow and vegetation surfaces. These two surface types exhibit somewhat different 3.7 μm clear sky reflectances and very different clear sky reflectances at 1.6 μm . However, their effect on the reflectance of thick clouds is minimal. The smooth curves represent approximate upper limits for ice cloud reflectance at each wavelength, valid for ψ values between 0° and 160° and for optically thick clouds. In the case of strong backscattering ($\psi > 160^\circ$), and in the case of thin clouds, the separation between water and ice cloud is less clear.

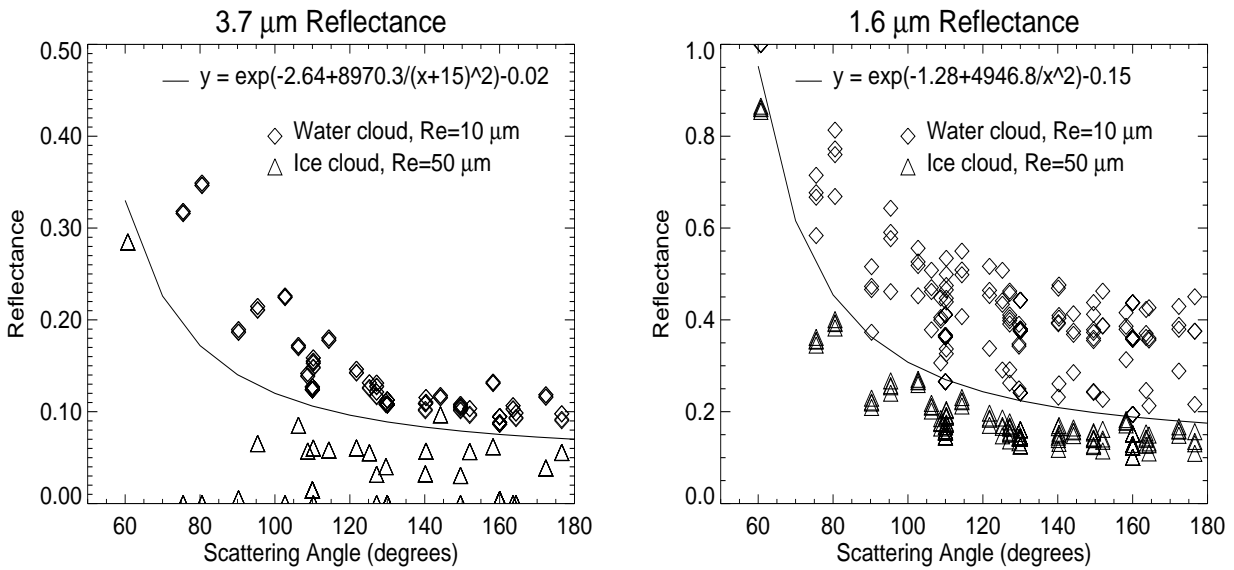


Figure 9. AVHRR channels 3 (3.7 μm) and 3A (1.6 μm) modeled reflectances as a function of scattering angle for water (diamond) and ice (triangle) clouds. All clouds have visible optical depths in the range 5-10. Also shown are the functions that approximately divide water and ice clouds at each of the two wavelengths. Calculations were done using midlatitude summer conditions.

Procedures

The phase algorithm starts by exploiting the physical property that only ice crystals will exist below some threshold temperature and only liquid droplets will exist above some other threshold temperature. For optically thick clouds the 11 μm brightness temperature will be very close to the kinetic temperature and simple temperature thresholds can be used to distinguish particle phase. For example, if T_4 were less than some minimum value, $\gamma_{\text{min}} = 243 \text{ K}$ (-30 C), then an optically thick cloud would almost certainly be composed of ice crystals. Similarly, if T_4 were greater than some maximum value, $\gamma_{\text{max}} = 273 \text{ K}$ (0 C) then the cloud would be liquid. But for optically thin clouds surface emission is a significant part of the measured radiance, and the relationship between the surface temperature and T_4 must be considered. Using the two thresholds above there are four relationships between the surface temperature T_s and T_4 that can be exploited to determine the phase, as listed in Table 4.

Table 4. Phase assignment based on temperature relationships.

Condition	Phase
$T_s - \delta < \gamma_{\text{max}}$ and $T_4 > \gamma_{\text{max}}$	Liquid
$T_s - \delta > \gamma_{\text{max}}$ and $T_4 > T_s$	Liquid
$T_s - \delta > \gamma_{\text{min}}$ and $T_4 < \gamma_{\text{min}}$	Ice
$T_s - \delta < \gamma_{\text{min}}$ and $T_4 < T_s$	Ice

The clear sky temperature can be used as a proxy for T_s , although T_s will generally be somewhat

lower than the clear sky value during the day (negative cloud radiative effect) and somewhat higher at night. The clear sky surface temperature can therefore be adjusted by a small amount δ . At night $\delta = -2$ K and during the day $\delta = +2$ K in this study. The application of these four conditions constitutes the first step of phase determination. The tests in Table 4 do not handle water clouds with temperatures less than γ_{\max} or less than T_s , and ice clouds with temperatures greater than γ_{\min} or greater than T_s .

If no estimate of T_s is available then an alternate, though less robust, method would be to simply use simple thresholds.; e.g., if T_4 is less than 243 K (-30°C) then the cloud is ice and if T_4 is greater than 303 K (+30°C) then the cloud is liquid. Hutchison et al. (1997) use -40°C for the lower threshold but suggest that -30°C is probably a reasonable lower bound. They do not suggest an upper bound for liquid clouds.

The second step employs the spectral properties described in the previous section and is different for day and night conditions. It is applied to the cloudy pixels that were not labeled in the first step. At night the tests are intended to identify optically thick ice cloud, thick water cloud, and most thin water cloud. The tests are: (a) if $T_3 - T_4$ is less than -0.5 K then it is a water cloud and (b) if $T_3 - T_4$ is greater than +1 K and $T_4 - T_5$ is between 0 and 1 K then it is an ice cloud.

During the day the tests in the second step are based on the 3.7 or 1.6 μm reflectance characteristics, utilizing the two reflectance functions shown in Figure 9. Only pixels with ψ less than 160 degrees and $T_4 - T_5$ less than 1 K are evaluated, as reflectances for strong backscattering and thin clouds are ambiguous. Observed 3.7 or 1.6 μm reflectances less than the threshold function values indicate ice cloud; those greater than the function values are water cloud.

The last step is to label any pixels that were not handled by the previous two steps. A simple temperature threshold is employed: if the 11 μm brightness temperature is less than 258.16 K (-15°C) then the cloud phase is ice, otherwise it is liquid. Because of the low precision and high uncertainty in T_3 (and therefore $T_3 - T_4$) when temperatures are very low, all pixels with T_4 less than 230 K are labelled as ice.

Remaining Problems

The procedure described here labels all cloudy pixels as either ice (solid) or water (liquid). Multi-layer and mixed-phase clouds are not identified as such. This problem is particularly apparent in the case of an ice cloud over a water cloud during the day. If the ice cloud is cold the temperature tests (step 1) will label it as ice. The reflectance test (step 2) will not relabel it even though its reflectance is high. Ice over water multilayer clouds that are not labeled by the temperature tests will be labeled as water clouds by the reflectance test. In both cases the result is not incorrect, but is not completely correct either.

Incorrect results typically occur in two other situations. Very thin water clouds over snow/ice may be mislabelled due to the low reflectance of the underlying surface. The same will be true of clouds that occupy only a small proportion of a pixel, as often occurs for cumuliform clouds and cloud edges.

CLOUD OPTICAL DEPTH AND PARTICLE EFFECTIVE RADIUS

The retrieval of cloud optical and microphysical properties from the AVHRR or AVHRR-like wavelengths has a long history; only a sample of the literature is given here. Hunt (1973) demonstrated the sensitivity of cloud emittance to changes in optical depth and particle size at thermal wavelengths. Liou (1974) showed that cirrus optical properties varied between 11 and 12 μm . Arking and Childs (1985) describe a technique for extracting a microphysical model parameter from AVHRR data. Inoue (1985) used the split-window channels to estimate cloud optical depth with an implicit particle size, while d'Entremont (1986) detected low clouds and fog at night using the variation of the 3.7-11 μm difference with particle size. Using a radiative transfer model and ground-based lidar for validation, Stone et al. (1990) discuss the problem of retrieving cirrus cloud optical depth from radiance measurements. Lin and Coakley (1993) used AVHRR channels 4 and 5 to simultaneously solve for the emittance and cloud fraction. Ou et al. (1993) developed a method to derive optical depth, cloud top temperature, and effective

radius from nighttime observations in AVHRR channels 3 and 4. Baum et al. (1994) modeled brightness temperature differences for liquid and ice clouds over the ocean. A review of cloud observations using satellites is given by Rossow (1989).

The importance of cloud optical depth τ and the particle effective radius r_e for remote sensing lies in the fact that the optical properties of clouds used in the calculation of radiative fluxes, the single scattering albedo, the asymmetry parameter, and the extinction coefficient, are proportional to the optical depth and effective radius. Cloud optical depth (unitless) is a measure of the cumulative depletion of radiation as it passes through the cloud. It is related to the transmissivity t via

$$t = e^{-\tau} \quad (16)$$

and is a product of the volume extinction coefficient and the physical thickness of the cloud.

The particle effective radius for liquid droplets is the ratio of the third to second moments of the drop size distribution $n(r)$:

$$r_e = \frac{\int_0^{\infty} r^3 n(r) dr}{\int_0^{\infty} r^2 n(r) dr} \quad (17)$$

For ice crystals the size parameter is better termed the "mean effective size". It is based on the parameterization of Fu and Liou (1993), which was developed from ray tracing calculations for scattering by randomly-oriented hexagonal crystals. The mean effective size is defined as:

$$D_e = \left(\int_{L_{min}}^{L_{max}} D^2 L n(L) dL \right) / \left(\int_{L_{min}}^{L_{max}} D L n(L) dL \right) \quad (18)$$

where D is the width of an ice crystal, L is the length, $n(L)$ is the size distribution, and L_{min} and L_{max} are the minimum and maximum lengths of ice crystals, respectively. In CASPR, "effective radius" refers to these two size parameters.

Cloud optical depth retrievals are done using a comprehensive data base of modeled reflectances and brightness temperatures covering a wide range of surface and atmospheric conditions (Key, 1995). Figures 10 and 11 give a few examples of the modeled data used in the retrieval of cloud optical depth and particle effective radius.


The basic approach for daytime retrievals of water (liquid) cloud follows that of Nakajima and King (1990) as illustrated in Figure 10. In the presence of solar radiation the retrieval is done using the reflectance in channels 2 and 3 (or 3A for NOAA-16 and later). For ice clouds under solar illumination the channel 3 reflectance is so small that it is unreliable. So channels 4 and 5 are used to obtain a range of possible solutions and channel 2 is used to constrain the solution. A valid solution exists if the observed brightness temperatures and BTDs fall within the range of the modeled data. If no valid solution was found, MISSING values are assigned.

At solar zenith angles greater than about 75-80 degrees over bright surfaces, uncertainties in modeled radiances and in the calibration of AVHRR channels 1 and 2 are large. When the solar zenith angle is greater than 80 degrees but less than 90 degrees, and when the surface clear sky channel 2 reflectance is high, only channels 4 and 5 are used in the retrieval. Solutions are obtained for all cloud top temperatures in the modeled data, and the effective radius/optical depth pair for the lowest cloud (arbitrary) that had a valid solution is given as the result. If no valid solution was found, MISSING values are assigned. Figure 3 shows the latitudes and times of the year where solar zenith angles greater than 75 degrees are experienced.

For nighttime retrievals, brightness temperature differences for channels 3 (or 3B) and 4 and 4 and 5 are employed (Figure 11). Both methods are based on the fact that the optical properties of clouds are different at each of the wavelengths examined. All three thermal channels are used for both liquid or ice clouds. The lookup table of brightness temperature differences is constructed for three different cloud top heights: 850, 650, 500 mb for liquid clouds and 700, 500, and 300 mb for ice clouds. The retrieval is done for each cloud top in both thermal channel combinations (3, 4 and 4, 5). The solution is the channel 4, 5 retrieval where the difference between the retrievals from both channel pairs is smallest.

In the lookup table procedure, interpolation to the observed values of solar zenith angle (0-85 degrees), precipitable water (2987-29,879 g m⁻²), and surface visible albedo (daytime; 0.06-0.99) or temperature (nighttime; 228-283 K). Single values of aerosol optical depth (0.06) and total column ozone (325 Dobson units) are used in all cases. Bilinear interpolation is done between effective radius and optical depth value pairs in the lookup tables; i.e., between the four points of each polygon in Figures 10 and 11. Effective radii for liquid clouds are 2.5, 6, 10, 14, 20 μm and for ice clouds are 20, 40, 60, 90, 120 μm. Optical depth values are 0, 1, 2, 4, 10, 20, 50, 80, and 150, with a maximum nighttime value of 15 and an ice cloud maximum of 50. The optical depth maximum for ice clouds is a result of their relatively low water contents. All clouds are modeled as either water or ice, with no mixed-phase clouds or overlapping combinations. Of course, it is entirely possible to have a liquid cloud under an ice cloud with a total optical depth greater than 50. This possibility will be addressed in a future version of CASPR.

For the daytime retrievals the reflectance of the surface under the cloud is assumed to be known. Similarly, the surface temperature under the cloud is needed for the nighttime retrievals. Neither can be measured directly from the AVHRR so they must be estimated. The relationship between the clear and cloudy sky reflectances depends on the cloud optical depth, phase, and the particle size distribution, and the anisotropic and spectral reflectance characteristics of the surface. The cloudy sky surface temperature is related to the clear sky temperature through the cloud base temperature, the residence time of the cloud, and the turbulent fluxes. Given the complexity of these relationships, no attempt is made to relate clear and cloudy temperatures or reflectances. A kriging procedure is used to create relatively smooth surfaces from the existing clear sky reflectances and temperatures for each surface type in the image. These clear sky surfaces are used as proxies to the actual surface reflectance and temperature in the optical depth/effective radius retrievals. The effect of using the clear sky values in place of the cloudy sky values is probably minimal for the daytime retrievals. At night, however, the effect can be significant, generally resulting in a positive bias in optical depth (i.e., the optical depths are too large) because clear sky surface temperatures may be considerably lower than cloudy sky temperatures.

	<p>CAUTION</p> <p>Effective radius and optical depth retrievals for low sun (large solar zenith angle) conditions have a large uncertainty.</p>
---	--

CLLOUD WATER PATH

Cloud water path is not computed explicitly but a procedure is available (**cloudwp**) in CASPR. Water path is calculated by converting the optical depth to a geometrical cloud thickness then multiplying it by the the cloud water content:

$$WP = z \cdot WC = \frac{\tau}{\beta} WC \quad (19)$$

where WP is the water path (g m^{-2}), WC is the cloud water content or density (g m^{-3}), τ is the visible optical depth (unitless), and β is the volume extinction coefficient (m^{-1}). For a homogenous cloud $\tau = \beta z$. The value for water content is the same as that used in radiative transfer calculations for the optical depth/particle effective radius retrievals: 0.2 g m^{-2} for water (liquid) clouds and 0.07 g m^{-2} for ice clouds. The extinction coefficient is also the same as that used in the radiative transfer calculations and depends on the particle effective radius.

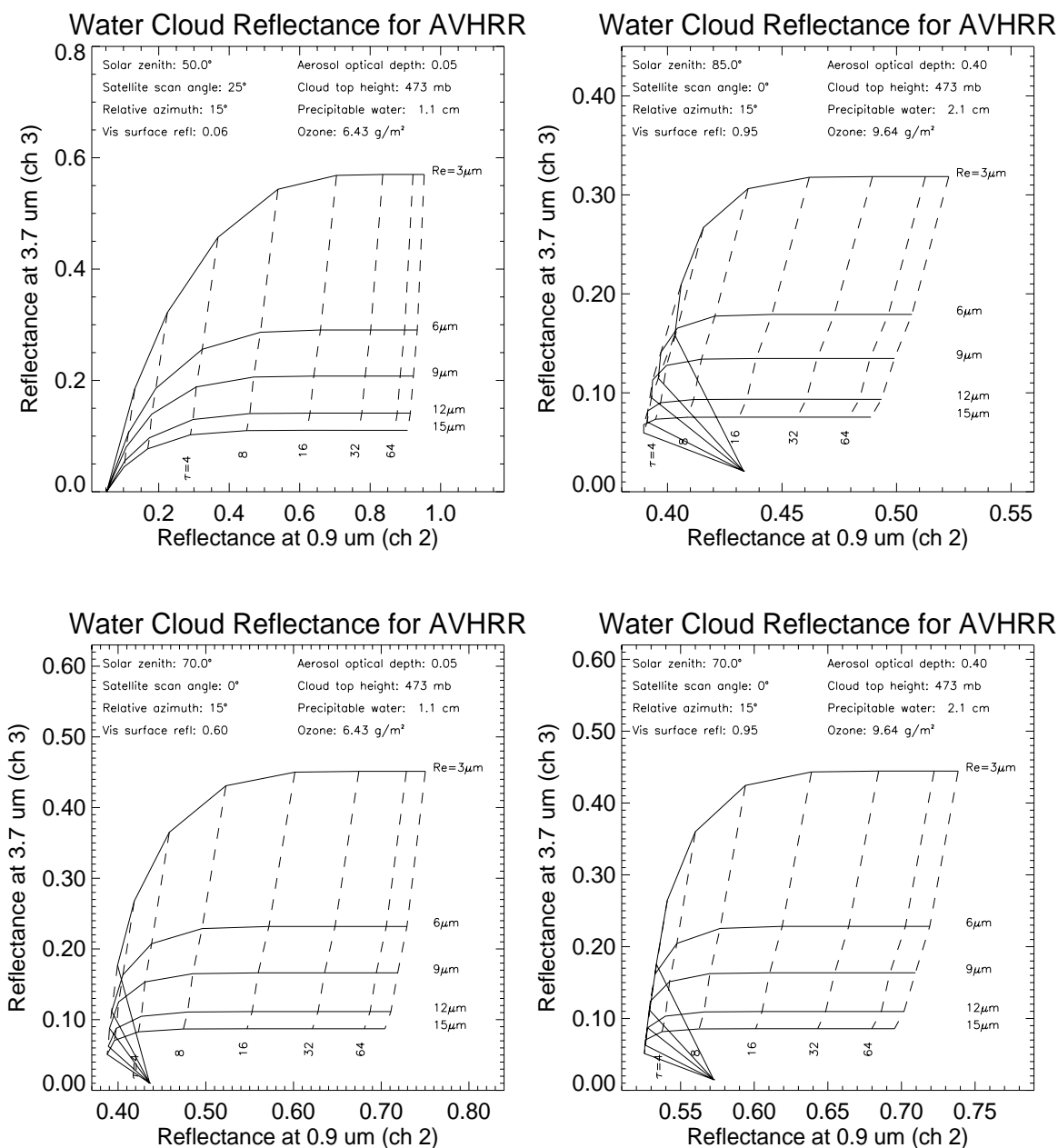


Figure 10. The relationship between two AVHRR reflective channels (2 and 3) as a function of water cloud optical depth and droplet effective radius over different surface types.

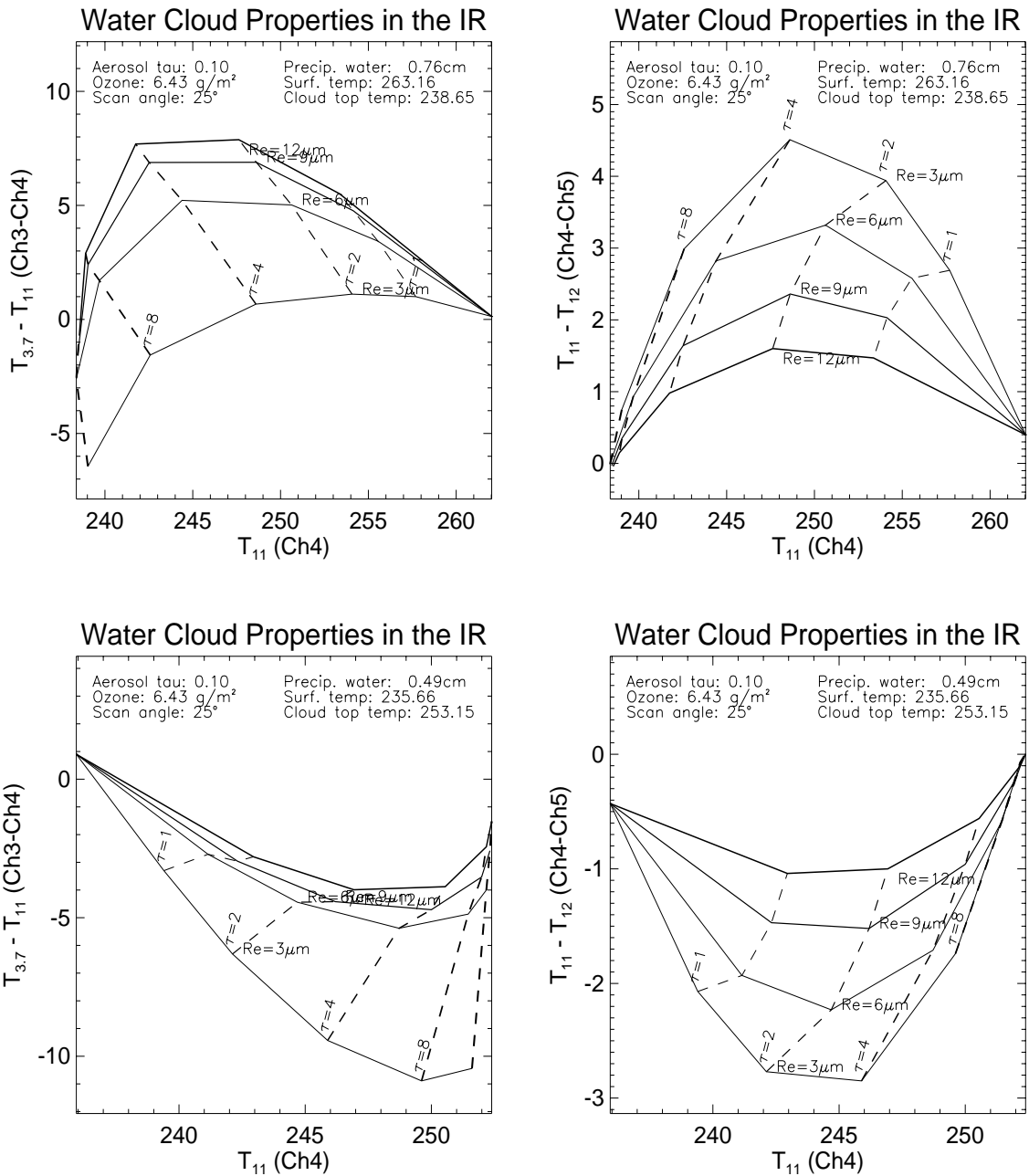


Figure 11. The relationship between the AVHRR channel 4 brightness temperature and the channels 4-5 difference as a function of water cloud optical depth and effective radius.

CLOUD TEMPERATURE AND PRESSURE

The cloud temperature is determined from the channel 4 brightness temperature, the clear sky brightness temperature (not corrected for the atmosphere), and the visible cloud optical depth. The infrared optical depth is determined from the visible optical depth using the parameterizations of cloud optical properties in (12). The thermal cloud optical depth, which in the retrieval is a nadir (vertical) optical depth, is converted to an optical depth along the slant (viewing) path by dividing it by the cosine of the sensor scan angle. If this adjusted cloud optical depth is less than some threshold, the brightness temperature is assumed to be a function of both the cloud temperature and the upwelling radiation from the surface and atmosphere below the cloud. The threshold is taken from the ISCCP processing scheme, chosen such that clouds with optical depths greater than the threshold have transmittances of less than 1% (equivalent to an optical depth of 4.6) and are considered opaque. For opaque clouds the cloud top temperature is simply the channel 4 temperature. If the cloud is not opaque, then the cloud temperature is determined by first computing the cloud transmittance t from the infrared optical depth with (13), then calculating the cloud radiance that would be required to produce the observed radiance of the cloudy pixel, given the cloud optical thickness and the observed clear sky radiance (as an approximation of the surface radiance under the cloud):

$$L_c = \frac{L_4 - tL_{clear}}{1 - t} \quad (20)$$

where L_c is the cloud radiance, L_4 is the channel 4 radiance, and L_{clear} is the clear sky radiance. If the estimated surface temperature is too low and the cloud is thin, then the cloud top temperature will be too high and vice versa. If the adjusted cloud top temperature is either lower than the tropopause temperature or higher than the maximum temperature from 950 mb to the tropopause, then it is reset to either the minimum or maximum temperature, as appropriate.

This scheme does not necessarily determine the cloud top temperature, but rather the effective radiating cloud temperature. While this may be close to the top temperature, it will generally represent a temperature somewhere beneath the cloud top. The differences between the retrieved cloud temperature and the actual cloud top temperature are illustrated in Figure 12 for two cases. For thin clouds the difference is greatest. Fortunately, the effect of this "error" on longwave radiative fluxes is small, because the thinner the cloud, the less is its influence.

The vertical location of the cloud, expressed as the cloud pressure, is determined by searching the temperature profile from the tropopause (or top of profile if below the tropopause) down. With this scheme, if a cloud has a temperature that could be either within or above an inversion, it will be placed below, i.e., closer to the surface (arbitrary). The physical thickness and cloud base height are determined from the cloud top height, the optical thickness, and an assumed cloud water content of 0.2 g m^{-3} for liquid clouds and 0.07 g m^{-3} for ice clouds.

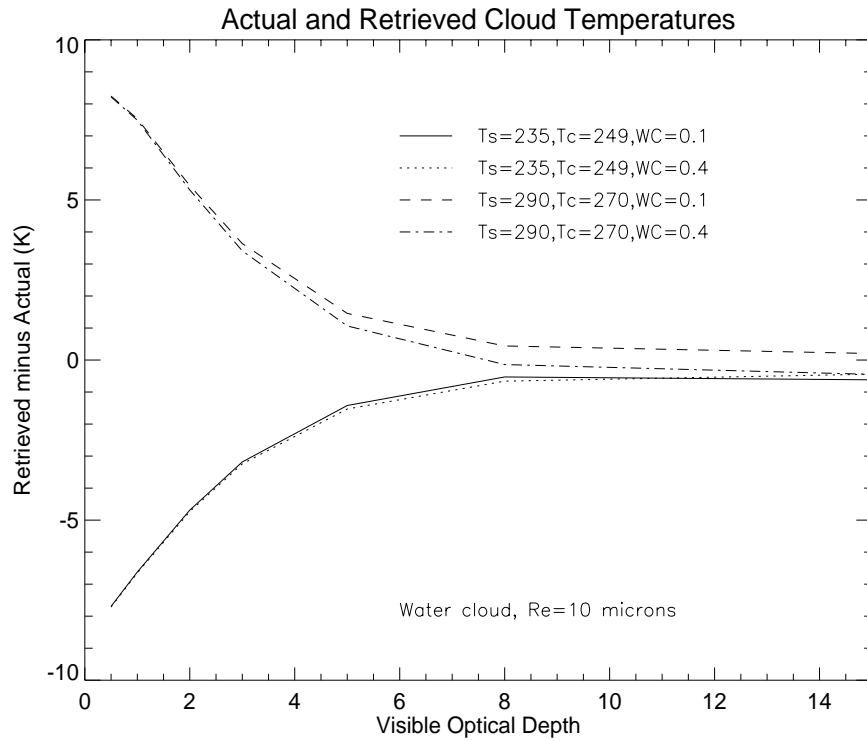



Figure 12. The difference between the retrieved cloud temperature and the actual cloud top temperature as a function of cloud optical depth. Differences are based on model simulations (Streamer) for two cloud-surface temperature relationships and for two cloud water contents (g m^{-3}).

7. RADIATIVE FLUXES

Upwelling and downwelling shortwave and longwave fluxes at the surface are computed with a neural network trained to simulate a radiative transfer model. The neural network, called FluxNet (Key and Schweiger, 1998), is also available as a stand-alone program. The radiative transfer model that FluxNet is trained to simulate is Streamer Key and Schweiger, 1998). FluxNet v4.0 is used in CASPR. Relative differences between the neural network and the radiative transfer model for surface radiative fluxes are shown in Figure 13. Errors in top-of-atmosphere fluxes are similar. FluxNet is 100 to 10,000 times faster than Streamer, and is nearly as accurate. See the Web pages at <http://stratus.ssec.wisc.edu> for more information.



CAUTION
FluxNet is very sensitive to out of range values.

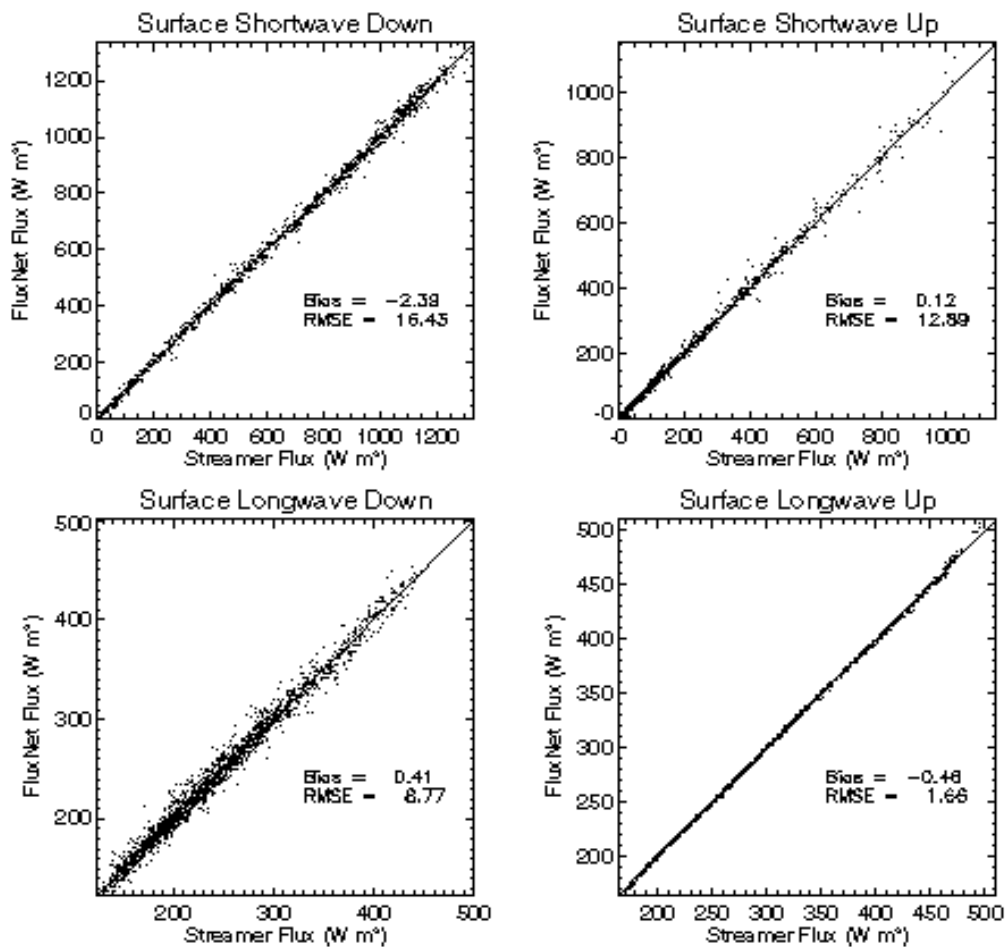


Figure 13. Comparison of FluxNet and Streamer fluxes for a wide range of atmospheric conditions.

The cloud radiative effect, more commonly called "cloud forcing", is computed from the net short-wave and longwave fluxes at the surface and TOA. It is defined as

$$CF_{\lambda, z} = \int_0^{A_c} \frac{\partial F_{\lambda, z}}{\partial a} da = F_{\lambda, z}(A_c) - F_{\lambda, z}(0) \quad (21)$$

where $F_{\lambda, z}$ is the net flux (W m^{-2}) for shortwave or longwave radiation (λ) at the surface and A_c is the cloud fraction in the scene. The net flux is equal to the downwelling minus the upwelling fluxes. Because pixels are assumed to be either completely cloudy or completely clear, the right side of the equation is simply the net flux (shortwave or longwave) for a cloudy pixel minus the net flux if the pixel were clear. The clear sky net flux for cloudy pixels is calculated with FluxNet by simply setting the cloud fraction to zero and other cloud properties to values used in training FluxNet for clear sky conditions. Analogous to net radiation, the all-wave net cloud forcing can be calculated from

$$CF_z = CF_{shortwave} + CF_{longwave} \quad (22)$$

The net all-wave cloud forcing is not calculated in CASPR.

8. REFERENCES

- Allen, Jr., R.C., P.A. Durkee, and C.H. Wash, 1990, Snow/cloud discrimination with multispectral satellite measurements. *J. Appl. Meteorol.*, 29(10): 994-1004.
- Arking, A. and J.D. Childs, 1985, Retrieval of cloud cover parameters from multispectral satellite images, *J. Climate Appl. Meteorol.*, 24: 322-333.
- Baum, B.A., R.F. Arduini, B.A. Wielicki, P. Minnis, and S.-C. Tsay, 1994, Multilevel cloud retrieval using multispectral HIRS and AVHRR data: Nighttime oceanic analysis, *J. Geophys. Res.*, 99(D3): 5499-5514.
- Csiszar, I. and G. Gutman, 1999, Mapping global land surface albedo from NOAA AVHRR, *J. Geophys. Res.*, 104(D6), 6215-6228.
- d'Entremont, R.P., 1986, Low and mid-level cloud analysis using nighttime multispectral imagery, *J. Clim. Appl. Meteorol.*, 25: 1853-1869.
- DeAbreu, R.A., J. Key, J.A. Maslanik, M.C. Serreze, and E.F. LeDrew, 1994, Comparison of *in situ* and AVHRR-derived surface broadband albedo over Arctic sea ice. *Arctic*, 47(3): 288-297.
- Dozier, J. and S.G. Warren, 1982, Effect of viewing angle on the infrared brightness temperature of snow, *Water Resources Res.*, 18(5), 1424-1434.
- Ebert, E.E., 1987, A pattern recognition algorithm for distinguishing surface and cloud types in the polar regions, *J. Climate Appl. Meteorol.*, 26: 1412-1427.
- Ebert, E.E. and J.A. Curry, 1992, A parameterization of ice cloud optical properties for climate models, *J. Geophys. Res.*, 97(D4): 3831-3836.
- Fu, Q. and K.N. Liou, 1993, Parameterization of the radiative properties of cirrus clouds, *J. Atmos. Sci.*, 50(13), 2008-2025.
- Gustafson, G.B. et al., 1994, Support of Environmental Requirements for Cloud Analysis and Archive (SERCAA), Phillips Laboratory, Hanscom Air Force Base, Scientific Report No. 2, PL-TR-94-2114,; 100 pp.
- Hu, Y.X. and K. Stamnes, 1993, An accurate parameterization of the radiative properties of water clouds suitable for use in climate models, *J. Climate*, 6(4): 728-742.
- Hunt, G.E., 1973, Radiative properties of terrestrial clouds at visible and infra-red wavelengths, *Quart. J. Roy. Meteor. Soc.*, 99: 346-349.
- Inoue, T., 1985, On the temperature and effective emissivity determination of semitransparent cirrus clouds by bi-spectral measurements in the 10 μm window region, *J. Meteorol. Soc. Japan*, 63: 88-99.
- Key, J., X. Wang, J. Stroeve, C. Fowler, 2001. Estimating the cloudy sky albedo of sea ice and snow from space. *J. Geophys. Res.*, in press.
- Key, J. and J. Intrieri, 2000, Cloud particle phase determination with the AVHRR, *J. Appl. Meteorol.*, 36(10), 1797-1805.
- Key, J. and A.J. Schweiger, 1998, Tools for atmospheric radiative transfer: Streamer and FluxNet. *Computers and Geosciences*, 24(5), 443-451.
- Key, J., A.J. Schweiger, and R.S. Stone, 1997, Expected uncertainty in satellite-derived estimates of the high-latitude surface radiation budget. *J. Geophys. Res.*, 102(C7), 15837-15847.

- Key, J., J. Collins, C. Fowler, and R.S. Stone, 1997, High-latitude surface temperature estimates from thermal satellite data, *Remote Sensing Environ.*, 61: 302-309.
- Key, J. and R.G. Barry, 1989, Cloud cover analysis with Arctic AVHRR, part 1: cloud detection, *J. Geophys. Res.*, 94 (D15): 18521-18535.
- Koepke, P., 1989, Removal of atmospheric effects from AVHRR albedos, *J. Appl. Meteorol.*, 28: 1341-1348.
- Li, Z. and L. Garand, 1994, Estimation of surface albedo from space: A parameterization for global application, *J. Geophys. Res.*, 99(D4), 8335-8350.
- Lin, X. and J.A. Coakley, Jr., 1993, Retrieval of properties for semitransparent clouds from multispectral infrared imagery data, *J. Geophys. Res.*, 98: 18501-18514.
- Lindsay, R.W. and D.A. Rothrock, 1994, Arctic sea ice albedo from AVHRR, *J. Climate*, 7(11): 1737-1749.
- Nakajima, T. and M.S. King, 1990, Determination of the optical thickness and effective particle radius of clouds from reflected solar radiation measurements. Part I: theory, *J. Atmos. Sci.*, 47(15): 1878-1893.
- NOAA, 1991, *NOAA Polar Orbiter Data User's Guide*, U.S. Dept. of Commerce., National. Ocean. and Atmos. Admin., NESDIS, February.
- Ou, S.C., K.N. Liou, W.M. Gooch, and Y. Takano, 1993, Remote sensing of cirrus cloud parameters using advanced very high resolution radiometer 3.7 and 10.9 μm channels, *Appl. Opt.*, 32: 2171-2180.
- Rao, C.R.N., 1993, Degradation of the visible and near-infrared channels of the advanced very high resolution radiometer on the NOAA-9 spacecraft: assessment and recommendations for corrections. NOAA Technical Report NESDIS 70, U.S. Department of Commerce, 25 pp.
- Rossow, W.B., 1989, Measuring cloud properties from space: A review, *J. Climate*, 2: 201-213.
- Rossow, W.B. and L.C. Garder, 1993, Cloud detection using satellite measurements of infrared and visible radiances for ISCCP, *J. Climate*, 6(12): 2341-2369.
- Sakellariou, N.K., H.g. Leighton, and Z. Li, 1993, Identification of clear and cloudy pixels at high latitudes from AVHRR radiances, *Int. J. Remote Sensing*, 14(10): 2005-2024.
- Saunders, R.W. and K.T. Kriebel, 1988, An improved method for detecting clear sky and cloudy radiances from AVHRR data, *Int. J. Remote Sensing*, 9(1), 123-150.
- Stamnes, K., S.C. Tsay, W. Wiscombe and K. Jayaweera, 1988, Numerically stable algorithm for discrete-ordinate-method radiative transfer in multiple scattering and emitting layered media, *Appl. Opt.*, 27: 2502-2509.
- Stone, R.S., G.L. Stephens, C.M.R. Platt, and S. Banks, 1990, The remote sensing of thin cirrus cloud using satellites, lidar, and radiative transfer theory, *J. Appl. Meteorol.*, 29(5): 353-366.
- Stowe, L.L., E.P. McClain, R. Carey, P. Pellegrino, and G.G. Gutman, 1991, Global distribution of cloud cover derived from NOAA/AVHRR operational satellite data, *Adv. Space Res.*, 11(3), 51-54.
- Suttles, J.T., R.N. Green, P. Minnis, G.L. Smith, W.F. Staylor, B.A. Wielicki, I.J. Walker, D.F. Young, V.R. Taylor, and L.L. Stowe, 1988, Angular radiation models for Earth-Atmosphere system. Volume I-Shortwave radiation, *NASA Reference Publication 1184*, 144 pp.
- Taylor, V.R. and Stowe, L.L., 1984, Atlas of reflectance patterns for uniform earth and cloud surfaces (NIMBUS-7 ERB-61 days), NOAA Technical Report NESDIS 10, U.S. Department of Commerce, 66 pp.

- Toon, O.B. C.P. McKay, and T.P. Ackerman, 1989, Rapid calculation of radiative heating rates and photo-dissociation rates in inhomogeneous multiple scattering atmospheres, *J. Geophys. Res.*, 94(D13): 16287-16301.
- Tsay, S.-C., K. Stamnes and K. Jayaweera, 1989, Radiative energy budget in the cloudy and hazy Arctic. *J. Atmos. Sci.*, 46: 1002-1018.
- Welch, R.M., S.K. Sengupta, A.K. Goroch, P. Rabindra, N. Rangaraj, and M.S. Navar, 1992, Polar cloud and surface classification using AVHRR imagery: An intercomparison of methods, *J. Appl. Meteorol.*, 31: 405-420.
- Yamanouchi, T., K. Suzuki, and S. Kawaguchi, 1987, Detection of clouds in Antarctica from infrared multispectral data of AVHRR. *J. Meteorol. Soc. Japan*, 65(6): 949-961.

9. REVISION HISTORY

The table below lists the most important changes for each major version (vX.) and minor version (vX.Y). For bug fix releases (vX.Y.Z) and changes, see the detailed revision history at the web site.

Version	Date	Description
v4.0	18 Jan 2002	Added surface shortwave and longwave cloud forcing variables; added netCDF input/output procedures; added more NOAA-15 and -16 capabilities (surface temperature and cloud detection); updated to FluxNet v4; removed the requirement that radiative flux calculations require profiles; made low sun cloud optical depth retrievals more restrictive, and questionable particle size/optical depth retrievals are now set to missing (no data is better than bad data); rewrote the procedure to calculate cloud water path; more modifications to cloud masking, e.g., added the cloud cloud and clear tests; added the <i>full_landmask</i> keyword; added the capability to supply a different surface type mask for each image in a time series; rewrote the clear sky compositing, allowing for an input clear sky image; revised, as part of the clear compositing rewrite, the clear sky statistics procedures in cloudmask_n ; revised the daytime part of the cloud phase retrieval; updated the cloud optical depth lookup tables with results from Streamer v3.0; removed the dependence of aerosol optical depth input on location; numerous plotting changes including a revamping of image plotting; removed the calibration (channels 1 and 2) procedure; added procedures to extract values along a line of latitude or longitude.
v3.2	10 Feb 2001	Significant improvements to both single-image and time series masking; allows for a variable number of profile levels at each grid point; allows for a grid of total column ozone; allows for a "complete" surface mask (all surface types: LAND, OCEAN, ICE, and SNOW) to be input; some improvements to display procedures; new test images from the AVHRR Polar Pathfinder project; other minor changes.
v3.1	7 Feb 2000	Modified the single image cloud mask, particularly at night; added a clear sky "composite" for use with time series; redesigned the display procedures so that individual windows are used for each parameter;; renamed three procedures; updated the calibration coefficients and central wavenumbers and added NOAA 14; added NOAA 15 surface temperature support (other procedures for NOAA 15 are not implemented).
v3.0	27 Oct 1999	Redesigned surface albedo retrieval; upgraded FluxNet to v3.0 and added TOA fluxes; added cloudy sky surface temperature; changed optical depth retrieval for low sun angles; fixed bugs in cloud phase averaging.
v2.5	6 Apr 1999	Added computation of precipitable water from profiles; fixed major problem with <i>FluxNet</i> (that WC isn't really variable); fixed times series display problems.

v2.4	25 Feb 1999	Revised the cloud detection algorithms (thresholds and clear sky composites); changed re/tau interpolation for daytime liquid; added/modified some utilities .
v2.3	1 Jan 1999	Changed (refined) cloud particle phase algorithm.
v2.2	27 Aug 1998	Refined optical depth tables, fixed bugs.
v2.2B (beta)	5 Jul 1998	Added Earth-Sun distance correction; added type checking on IDL-C calls; improved cloud masking (single-image and time series); rewrote optical depth/effective radius retrieval.
v2.1B (beta)	20 Aug 1997	Redesigned neural networks to do only cloud optical depth and particle effective radius, and went back to original cloud temperature algorithm. Cleaned up the display procedures.
v2.0B (beta)	4 Aug 1997	Recoded many procedures to operate on arrays, some procedures are now in C; replaced the cloud tau, Re, Tc algorithm; eliminated the option to compute fluxes with Streamer; eliminated internal mean profiles; reduced the number of parameter categories, removed subsampling from caspr.

v1.11	1 Aug 1996	Implemented no_warn; fixed minor bugs.
v1.1	25 Jul 1996	Replaced parameterized flux scheme with FluxNet, added snow-free land surface temperature retrieval (v1.02), modified optical depth retrieval (v1.06).
v1.0	1 Jan 1996	Minor changes; much debugging.
v1.0A (alpha)	26 Jun 1995	First release.

